Meanders of the Gulf Stream Downstream from Cape Hatteras 1975–1978

GEORGE R. HALLIWELL, JR.[1]

College of Marine Studies, University of Delaware, Lewes, DE 19958

CHRISTOPHER N. K. MOOERS

Department of Oceanography, Naval Postgraduate School, Monterey, CA 93940

(Manuscript received 10 April 1982, in final form 17 March 1983)

ABSTRACT

Weekly Gulf Stream paths within 1000 km downstream of Cape Hatteras were obtained for 1975–78 from the Navy's weekly EOFA charts based on satellite IR imagery. They displayed two dominant meander modes: first, a standing meander energetic over periods between 4 months and at least 4 years; and second, downstream-propagating meanders that were most energetic at periods of several weeks. The long-period standing meander was confined between nodes located at the separation point near Cape Hatteras (i.e., where the Stream's mean path turns seaward) and at a point about 600 km farther downstream. The rms amplitude was 36 km at the antinode. The amplitude of propagating meanders increased rapidly in the first 200 km downstream of the separation point, where the capture of warm-core eddies was common. Farther downstream, the predominant meanders had a wavelength averaging 330 km, a period averaging 1.5 month, a phase speed averaging 8 cm s^{-1}, a downstream group speed averaging 17 cm s^{-1}, and downstream exponential spatial growth rate averaging 3.2×10^{-3} km^{-1}. They were energetic over a broad wavenumber-frequency band (periods of 1–6 months and wavelengths of 200 to more than 800 km) due to variable wavelengths, propagation speeds, and inter-meander space and time scales. The energetic wavenumber band was broadest near 4 cpy; it narrowed and shifted to larger wavenumbers with increasing frequency. The amplitude and frequency of occurrence of propagating meanders had large variability over time scales of a few months and longer.

1. Introduction

As the Gulf Stream flows northeastward past Cape Hatteras, it separates from the continental margin and turns seaward. Downstream of this separation point (SP), the Stream often meanders hundreds of kilometers about its mean path. These meanders have a wide range of space and time scales. At superinertial periods, they have time scales of one day to several months, with properties that depend on the period. At periods of one to several days, the dominant meanders have wavelengths and amplitudes of several tens of kilometers and propagate downstream at 5 to 25 cm s^{-1} (Robinson *et al.*, 1974). At periods between two weeks and several months, meanders have wavelengths between 200 and 400 km and amplitudes reaching 100 to 200 km and they propagate downstream at 5 to 10 cm s^{-1} (Hansen, 1970). In a least-squares spectrum of satellite-derived positions of the Stream at 70°W with an irregular sampling rate in time (Maul *et al.*, 1978), there were peaks for two period bands: 18–22 days and 30–90 days; fluctuations were also energetic at periods greater than 120 days.

The present analysis is a continuation of the statistical analyses of the Gulf Stream surface temperature front using weekly positions obtained from the Experimental Ocean Frontal Analysis (EOFA) charts of NAVOCEANO, reported in Halliwell and Mooers (1979) (hereafter referred to as HM). Using weekly positions of the front as a measure of stream path, only the meanders with periods greater than two weeks could be studied. Hence, the shorter-period meanders observed by Robinson *et al.* (1974) were unresolved. We refer to meanders with periods between two weeks and four months, as "short period" meanders, essentially those described by Hansen (1970). Similarly, we refer to meanders with periods longer than four months as "long-period meanders."

The analysis presented in HM has been expanded upon in several significant ways. The Gulf Stream grid overlayed on the EOFA charts was extended to the southwest, placing the western edge near the longitude of Cape Hatteras and increasing the alongstream length of the grid from 810 to 990 km. The resolution was increased by a factor of 3 in the alongstream direction, and by a factor of 2.5 in the cross-stream direction. Finally, a four-year data set

[1] Present affiliation: School of Oceanography, Oregon State University, Corvallis, OR 97331.

was used (January 1975–December 1978), which extends the two-year data set analyzed in HM.

These improvements allowed substantial new information about the mean Stream path and its variability to be extracted. Improved estimates of propagating meander parameters were made and compared to other estimates. The structure of the long-period meanders was characterized as standing waves. A fixed separation point (SP) southeast of Cape Hatteras (near 35°20′N, 74°50′W for the surface temperature front) was identified. At SP, the Stream begins to cross isobaths toward deeper water and has a local minimum in the variance of path fluctuations.

The data are described first, followed by a summary of the basic statistics of the Gulf Stream front. A time-domain empirical orthogonal function (EOF) analysis of the front is then used to separate the variance due to long-period, standing meanders from that due to short-period, propagating meanders, which sets the stage for the subsequent analyses.

2. The data

The new Gulf Stream grid overlayed on the EOFA charts (Fig. 1) has several differences from the grid used in HM. Both grids are based on the same reference line which connects 36°N, 75°W with 39°N, 70°W and is oriented approximately along the mean path of the Stream south of New England and Georges Bank. The x (cross-stream) coordinate is zero along this line and positive seaward, with a 10 km resolution used in gridding data. The y (alongstream) coordinate is zero at the upstream end of the grid and positive downstream, with a 30 km resolution used in gridding data. (The HM grid resolution was 25 km cross-stream and 90 km alongstream. The origin of the HM grid was the point $x = 0$, $y = 180$ km in the new grid.)

Displacements of the Gulf Stream surface temperature front from the line $x = 0$ were measured weekly at each alongstream grid point from 1 January 1975 to 31 December 1978 (209 weeks). The displacement of the front from $x = 0$ was measured to a five km resolution, five times more precise than the measurements discussed in HM.

The preparation of the EOFA charts and a discussion of the expected errors were presented in HM. A brief summary is given here. The EOFA charts were subjectively prepared by a human analyst, using satellite IR images and SST measurements from ship and aircraft to best locate the fronts on the date of chart issue, cf HM for a sample chart. Perchal (1976) estimated that the frontal positions on each chart were located within five to ten km of their actual positions in regions where good satellite images of the front were available and 20 to 40 km where not. These errors could not be accurately quantified. Occasionally, portions of the surface front could not be ac-

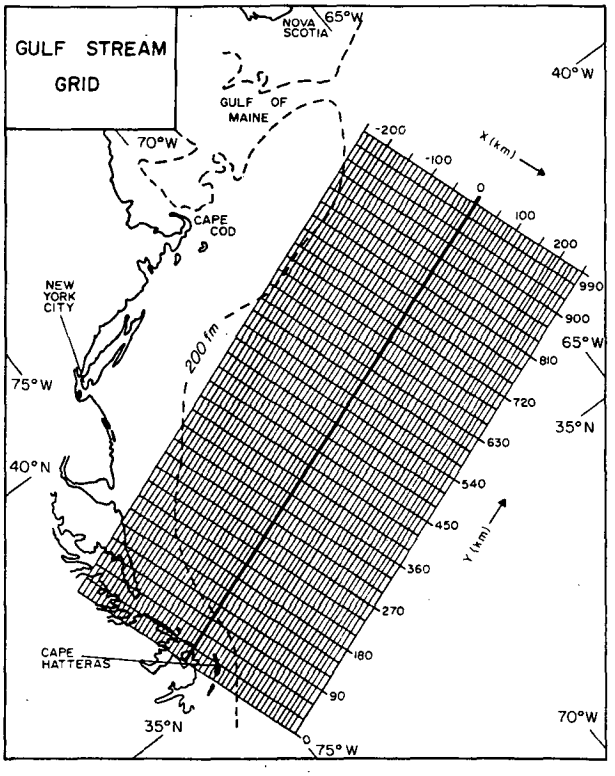

FIG. 1. The Gulf Stream grid.

curately located from satellite images for durations of a fortnight or longer, due to cloud cover or sea smoke and haze.

Thus, frontal positions on the EOFA charts generally were obtained from satellite image fixes unequally spaced in time. However, the EOFA analyst always attempted to estimate frontal positions on the date of chart issue and, hence, to decrease the effects of the uneven position fixes. Thus, the noise in the EOFA data is not purely random. We could not accurately quantify the EOFA errors in our time series *a priori* due to this irregular sampling and human subjectivity, but some insight was obtained from the theory of uneven sampling intervals, or "jitter." Otnes and Enochson (1978) characterized the noise introduced by jitter for two cases: first, the sampling time error is uniformly distributed within a time window Δt centered on the average sampling time; and second, the sampling time error has a Gaussian distribution about the average sampling time. In both cases the noise introduced has two components, a white component and a frequency-dependent component with the noise variance increasing with increasing frequency. Since the spectra of the Stream displacements were red, the signal-to-noise ratio for the more-energetic lower frequencies may not have been seriously affected by the jitter.

We felt justified in proceeding with this analysis of a unique four-year space-time data set of the Stream since it likely contained important new information about Gulf Stream meanders. Evaluation of the results *a posteriori* presented here and in HM confirmed our optimism for three reasons:

1) Wherever our estimates of meander parameters could be compared to existing observations or estimates, the comparisons were always excellent.

2) Aliasing of variance from motions at periods shorter than the Nyquist (two weeks) appeared not to be serious since the amplitudes of the higher-frequency meanders were substantially smaller than those of the lower-frequency meanders that we studied.

3) The signal-to-noise ratio increased with decreasing frequency and it was large enough to clearly enable resolution of the energetic wavenumber-frequency bands of meanders with frequencies equal to or less than those characteristic of the most energetic downstream-propagating meanders ($\leq$12 cpy).[2]

Between frequencies of 12 and 26 cpy the signal-to-noise ratio was relatively poor. To improve the ratio for our analyses, we estimated meander parameters using time series that were partially "denoised" through empirical orthogonal function decomposition.

Nevertheless, caution must still be used in interpreting the results presented here. Error bars are presented for all spectra. Since errors in general could not be fully quantified, we qualitatively estimated the degree of confidence we had in our conclusions and estimates of meander parameters. These estimates are presented along with the discussions of the meanders.

One problem in digitizing the frontal positions had to be dealt with subjectively. Some meanders became very large and "S" shaped, resulting in a multiple-valued frontal locus. In these cases, the front was minimally but subjectively smoothed to produce a single-valued frontal locus, and then digitized.

By necessity, we used the surface temperature front to locate the path of the Stream. The conventional index of the path is the location of the 15°C isotherm at a depth of 200 m (Fuglister and Voorhis, 1965), which is usually located beneath the axis of the current jet. The surface front is located on average about 15 km shoreward of this index, Hansen and Maul (1970). Variability in the cross-stream structure of the Stream, due in large part to synoptic scale atmospheric forcing, results in variability in the shoreward displacement of the surface front from the index (Curtin *et al.*, 1978). This variability, with a maximum range in displacement of only a very few tens of kilometers, has substantially smaller amplitude and substantially higher frequencies than the meanders considered here. Thus, it probably does not seriously degrade the data for present purposes.

3. Basic statistics of the Gulf Stream front

The standard deviation of Stream fluctuations had a relative minimum at y = 60 km, the location of SP, Table 1. The mean path downstream of this point, together with the long-period meanders, will be discussed in Section 5. Downstream of SP the standard deviation and the range of extreme positions increased to a relative maximum at y = 180 km, near which the capture of warm-core eddies by the Stream was frequent, Fig. 2. (Only warm-core eddies were analyzed, since their life histories were easily tracked on the EOFA charts; cold-core eddies were much more difficult to track.) However, capture of cold-core eddies by the Stream can also generate meanders downstream of Cape Hatteras, Watts and Olson (1978). Farther downstream there was a relative minimum in standard deviation between y = 210 and 240 km. The standard deviation and range of extreme positions generally increased from y = 240 to 690 km. In this interval, the formation and capture of warm-core eddies was uncommon. A relative maximum in the standard deviation and range of extreme positions occurred at y = 390 km, corresponding to a local maximum in the amplitude of the long-period

[2] cpy is cycles per year; on several spectra shown, cpw denotes cycles per week.

TABLE 1. Statistics of the cross-stream position of the Gulf Stream surface temperature front, 1975–78. The latitude and longitude of the separation point (SP) and the downstream node of the long-period standing meander (y = 690 km) are given.

Alongstream position (km)	Mean (km)	Standard deviation (km)	Minimum (km)	Maximum (km)	Range (km)
0	128	25	60	205	145
30	111	20	55	195	140
60 (SP) 35°20'N 74°50'W	88	14	35	120	85
90	65	19	5	110	105
120	47	24	−40	120	160
150	33	27	−85	100	185
180	18	35	−115	100	215
210	5	33	−85	95	180
240	−5	32	−100	85	185
270	−14	35	−125	80	205
300	−21	40	−170	90	260
330	−23	43	−190	100	280
360	−25	47	−215	125	340
390	−26	47	−220	125	345
420	−24	45	−230	85	315
450	−25	43	−235	80	315
480	−29	43	−235	65	300
510	−31	44	−225	75	300
540	−30	46	−250	85	335
570	−25	49	−240	115	355
600	−14	55	−150	180	330
630	−3	63	−170	260	430
660	6	65	−180	275	455
690 38°15'N 68°12'N	17	64	−200	280	480
720	15	66	−210	270	480
750	17	70	−205	260	465
780	14	80	−215	270	485
810	15	82	−230	270	500
840	22	82	−235	240	475
870	30	85	−235	235	470
900	37	92	−240	320	560
930	46	91	−240	310	550
960	51	86	−230	280	510
990	57	87	−220	265	485

standing meander as discussed in Section 5. The existence of this meander is illustrated by the temporal autocorrelation function of the Stream path contoured as a function of lag time and alongstream position, Fig. 3. The integral correlation time scale was greatest (10 weeks) at y = 390 km, and long-period fluctuations were evident between y = 180 and y = 690 km. In the interval 600 ≤ y ≤ 780 km, the downstream increase in standard deviation and range was greater than farther upstream or downstream. The range reached a relative maximum at y = 900 km. Formation and capture of warm-core eddies were common for y > 690 km.

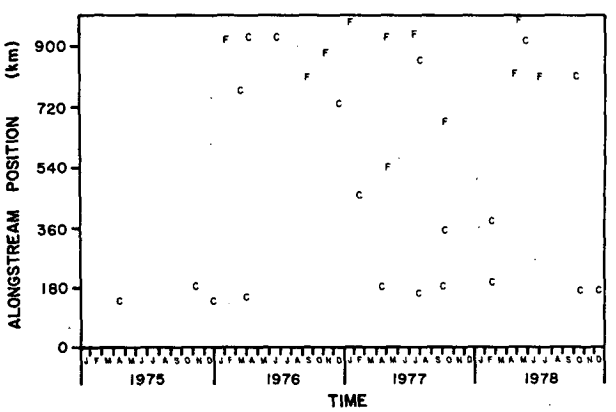

FIG. 2. Time and alongstream location of formation ("F") and capture ("C") of warm-core eddies.

These features suggested dividing the alongstream domain into several subdomains for analysis. Subdomain 1, 0 ≤ y ≤ 60 km, was located upstream of SP. Subdomain 2, 60 < y ≤ 240 km, contained the region of frequent capture of warm-core eddies. Subdomain 3, 240 < y ≤ 690 km, was rarely influenced by the formation or capture of warm-core eddies. Subdomain 4, 690 < y ≤ 990 km, was influenced by the frequent formation *and* capture of warm-core eddies.

4. Modal decomposition of the front

Empirical orthogonal function (EOF) analysis in the time domain was used to determine the structure

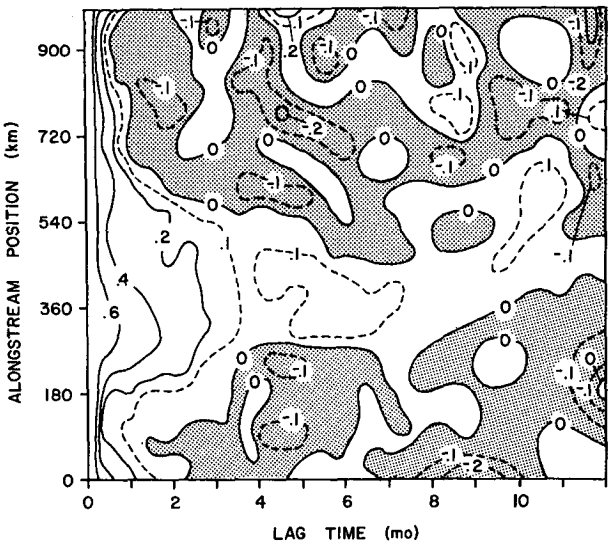

FIG. 3. Autocorrelation of the Gulf Stream surface temperature front as a function of lag time and alongstream position. Shaded regions indicate negative correlation.

of Gulf Stream meanders, *cf* HM. With the time series at 34 alongstream grid points, 34 modes were computed, each consisting of a spatial structure and corresponding time-varying amplitude. The first six modes (Fig. 4) accounted for 82% of the total variance in the 34 time series. The percent variance explained by Modes 1 through 6 was 25, 20, 13, 11, 8, and 5, respectively.

The normalized entropy was 0.66, compared to 0.78 in HM. This quantity, defined in HM, is a measure of the order in a given set of time series. For perfect order, the normalized entropy is zero, and one empirical mode accounts for all of the variance in all of the time series. For perfect disorder (for example, time series of incoherent random noise), the normalized entropy is one, and all empirical modes contain an equal fraction of the total variance. More order was therefore present in this four-year study, probably because the resolution of meanders with periods longer than four months produced a larger signal-to-noise ratio than for the two-year study analyzed in HM.

The dissimilarity of Mode 4 relative to the other first six modes is made evident by comparing its autospectrum to those of the other five, Fig. 5. Mode 4 described a standing meander energetic at periods greater than four months. Based on its red autospectrum, the signal-to-noise ratio of this mode was excellent at longer periods. This meander had an antinode at y = 390 km and nodes at SP and y = 690 km, with small amplitude upstream and downstream of the nodes, Fig. 4. At y = 390 km this mode accounted for about two-thirds of the path variance, and within 100 km upstream and downstream of y = 390 km it accounted for over 50% of the variance.

Modes 14 and 15 (Fig. 6) represented long-period meanders upstream of SP. They each explained less than 1% of the total variance in all of the time series, but together they explained about two-thirds of the variance at y = 0 km and y = 30 km, Fig. 6. Mode 14 was relatively energetic for periods between 2 and 12 months, and Mode 15 for periods greater than several months, Fig. 7. The peaks in the modal autospectra were statistically significant at a 95% confidence level. Long-period standing meanders thus existed both upstream (Modes 14 and 15) and downstream (Mode 4) of the SP, but they were apparently unrelated.

Modes other than 4, 14 and 15 were associated with propagating meanders and noise. Since empirical modes represent standing meanders, the variance due to propagating meanders appeared in several modes which when added together in space and time reproduced the propagating meanders. Modes 1, 2, and 3 represented about 75% of the variance due to the propagating meanders for y > 540 km, Fig. 4.

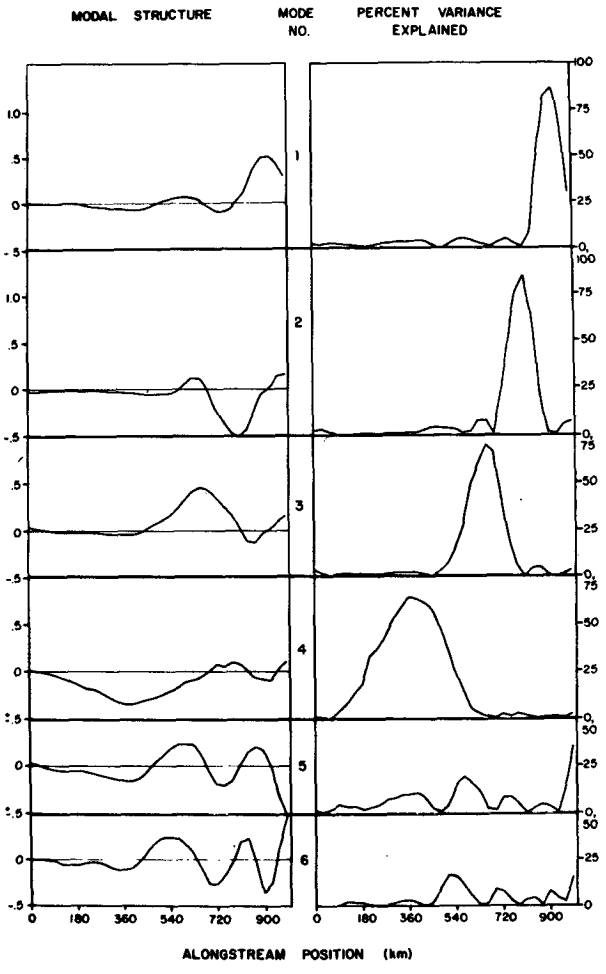

FIG. 4. The modal structure of, and percent variance explained by, the first six EOF modes in the time domain of the surface front.

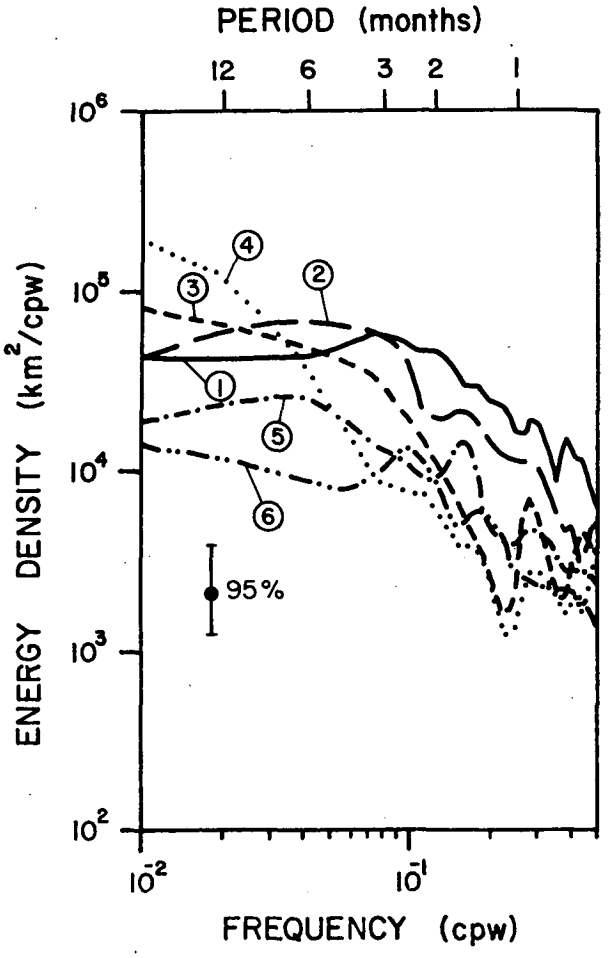

FIG. 5. Autospectra of the first six EOF modes in the time domain. The 95% confidence band is shown.

Their average wavelength was about 400 km. Their maximum amplitudes were each confined to the alongstream interval of one-half wavelength and displaced about one-quarter wavelength from each other. The maximum amplitude of Mode 1 was centered near $y = 930$ km, Mode 2 near $y = 810$ km and Mode 3 near $y = 690$ km. These modes were more energetic than Mode 4 at periods less than six months, Fig. 5. The remaining propagating meander variance was contained in Mode 5 and greater, excluding Modes 14 and 15. The frequency spectra became increasingly white for increasing mode number, indicating a decreasing signal-to-noise ratio.

5. Long-period standing meanders

a. The standing meander upstream of the separation point

The long-period meander upstream of SP was uncorrelated with the long-period meander farther downstream since it appeared in a separate EOF. We can only describe the temporal variability of the upstream meander near its downstream node at SP.

A time series at $y = 0$ containing variance due to the standing meander plus random noise was computed by summing Modes 14 and 15. The standard deviation of this reconstructed time series was 20 km, and the extreme shoreward and seaward displacements were −55 and 69 km for a total range of 124 km. Consequently, this meander may be influential on the outer shelf and slope off North Carolina and possibly farther south.

Based on their autospectra (Fig. 7), Modes 14 and 15 were about equally energetic at the annual period. For the reconstructed time series at $y = 0$, extreme monthly averaged displacements ranged from 12.9 km seaward of the mean position in March to 13.1 km shoreward of the mean position in June, Table 2. The mean displacement was 9.9 km seaward of the mean position from January through May and 4.9 km shoreward of its mean position from June through

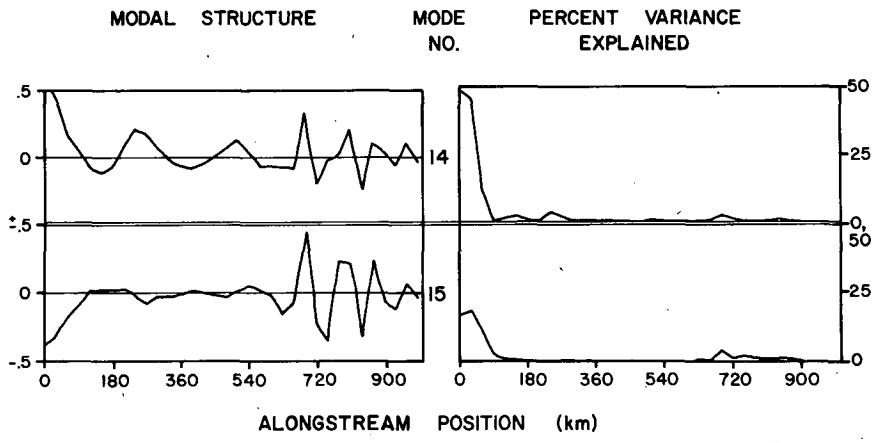

FIG. 6. The modal structure and percent variance explained by EOF Modes 14 and 15 in the time domain of the surface front.

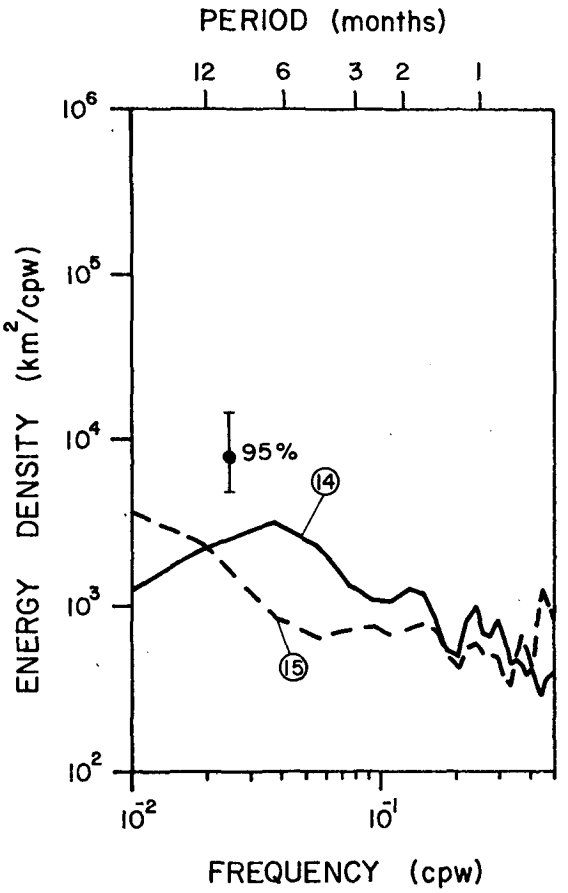

FIG. 7. Autospectra of EOF Modes 14 and 15 in the time domain.

December, Table 2, a statistically significant difference (95% confidence level). Thus, this meander mode probably had a weak annual cycle. The path also seemed to have a semiannual cycle (Table 2); it was located shoreward of its mean position during June through August and November through December and seaward during the other months.

b. The standing meander downstream of the separation point

Based on the reconstructed time series for Mode 4 at each grid point, the standard deviation and extreme position envelope, plotted (Fig. 8) about the mean path, illustrate the structure of this mode and its relationship to the mean path. The antinode of the meander was south of the New England shelf (at y = 390 km) where the rms amplitude was 36 km. The downstream node was at y = 690 km. Farther downstream the meander amplitude was small. There was an abrupt change in the direction of the mean path at the downstream node with the Stream turning about 20 degrees cyclonically. Except for this turn, the mean path curvature was everywhere anticyclonic,[3] but the magnitude of the curvature was greater in the domain of the standing meander than farther downstream. Essentially, a shoreward bulge in the mean path coincided with the domain of the standing meander.

TABLE 2. Monthly averages of Gulf Stream parameters. Mode 4 is represented by the amplitude at the antinode, y = 390 km, and the standing meander upstream of SP is represented by the amplitude at y = 0. The meander amplitude index is discussed in Section 6.

Month	Standing meander amplitude upstream of SP (km)	Mode 4 amplitude (km)	Meander amplitude index
Jan	7.4	14.3	0.12
Feb	11.7	19.9	0.16
Mar	12.9	−1.5	0.27
Apr	6.8	−0.5	0.27
May	10.5	−5.4	0.22
Jun	−13.1	−1.8	0.20
Jul	−4.3	−4.0	0.23
Aug	−3.3	8.8	0.35
Sep	2.6	−17.5	0.43
Oct	3.6	−23.8	0.22
Nov	−10.8	4.2	0.19
Dec	−9.1	3.9	0.22
Nov–Feb	−0.2	10.6	0.17
Mar–Oct	2.0	−5.7	0.27
Jan–May	9.9	5.3	0.21
June–Dec	−4.9	−4.3	0.26

Mode 4 did not represent all of the long-period variance in the Stream path downstream of the SP. The propagating meanders (Modes 1, 2 and 3) accounted for much of the long period variance downstream of y = 540 km, Figs. 4 and 5. Due to the influence of the propagating meanders at periods longer than a few months, the path of the Stream did not remain essentially stationary downstream of y = 690 km, as might be suggested by Fig. 8.

From winter through summer 1975 at the antinode of the standing meander, the Stream was located on average ~20 km shoreward of its mean position, Fig. 9. It was near its extreme seaward position throughout autumn and winter of 1975 to 1976, averaging about 60 km seaward of the mean path at the antinode. From spring 1976 through winter 1978, the Stream gradually shifted shoreward, but with superimposed

[3] Path curvature is measured with reference to a great circle path, which is not a straight line on a Mercator projection as used for the EOFA charts. A great circle path would have a small anticyclonic curvature on Fig. 8. The mean path of the Stream is oriented almost east-west at a latitude of 38.7°N near 65°W, the eastern edge of the analysis domain. A great circle path that reaches a maximum latitude of 38.7°N at 65°W would cross a latitude of 38.1°N near 75°W, the western edge of the domain. It is clear in proceeding westward along the mean path from 65°W in Fig. 8 that the anticyclonic curvature of the mean path is everywhere (except at y = 690 km) at least an order of magnitude greater than the anticyclonic curvature of a great circle path.

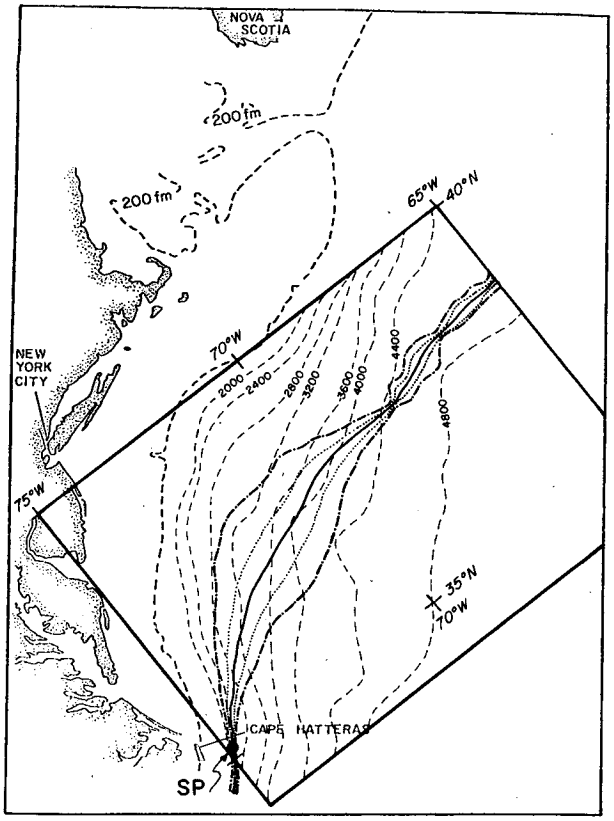

FIG. 8. Mean position, standard deviation envelope, and extreme position envelope of EOF Mode 4. SP is the separation point.

shorter-period fluctuations, averaging 80 km shoreward of the mean path at the antinode during January and February 1978. This interval included most of the two-year interval studied in HM. (A shoreward trend of 60 km in the mean position of the Stream south of New England was noted in HM.) After winter 1978, the Stream fluctuated about its mean position with a period of several months.

A distinct annual cycle was not evident in either the time-varying amplitude or the autospectrum of Mode 4. However, at its antinode the maximum monthly-average shoreward displacement was −23.8 km in October, and the maximum monthly average seaward displacement was 19.9 km in February, Table 2. The mean displacement from November through February was 10.6 km seaward of the mean position, and the mean displacement from March through October was 5.7 km shoreward of the mean position, a difference that was statistically significant at the 95% confidence level. Hence, there was a weak annual cycle associated with this standing meander.

c. Other reports of long-period path and transport fluctuations

From approximately monthly Gulf Stream positions near NDBO Environmental Data Buoy EB01 (36°30′N, 73°30′W or ~300 km downstream of the SP) determined from January 1971–August 1972, path fluctuations had time scales of several months (Parker, 1976). From submarine cable measurements, the Florida Current transport fluctuations also had time scales of several months between April 1952 and June 1953, Stommel (1966).

There is an annual transport cycle in each of the several segments of the Gulf Stream System from the Caribbean to the Grand Banks, with a minimum in autumn and a maximum in summer and with a downstream phase lag of a few weeks from the Caribbean to beyond Cape Hatteras (Fuglister, 1951). Least-squares spectra of Florida Current transport from several studies all had an annual peak (Maul *et al.*, 1978). Farther upstream the Loop Current migrates northward in spring and summer and southward in autumn and winter (Maul, 1977). In the present study, the long-period standing meanders of the Stream path upstream and downstream of SP had only a small annual cycle amplitude. The relationship of these various indicators of an annual cycle to the Gulf Stream System in general, and the long-period meander in particular, warrants further study.

d. Dynamics of the standing meander downstream of the separation point

Two classes of dynamics can influence the Stream path and the location of separation in the vicinity of Cape Hatteras: 1) large-scale (basin-wide) dynamics,

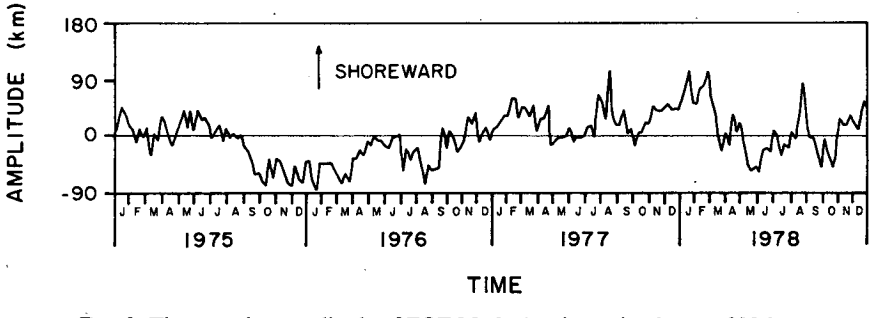

FIG. 9. Time-varying amplitude of EOF Mode 4 at its antinode, y = 390 km.

and 2) local path dynamics. The large-scale dynamics primarily include the effects of variable wind stress curl and thermalhaline forcing over the North Atlantic basin. The local path dynamics primarily includes the effects of bottom topography, the volume transport and inertia of the Stream, latitudinal variation in the Coriolis parameter, and regional wind stress curl and thermalhaline forcing in the vicinity of the Stream (from the northern Sargasso Sea to the continental margin). The local path dynamics are not independent of the large-scale dynamics because some parameters affecting local path dynamics are influenced by, or related to, the large-scale forcing.

Inertial theories of the Gulf Stream predict that SP is located near the latitude of zero wind stress curl (Charney, 1955, and Morgan, 1956). At the western edge of the North Atlantic Basin the contour of zero curl is located on average near the latitude of Cape Hatteras (Leetmaa and Bunker, 1978). According to Veronis (1973) the thermocline must be shallower on the western than on the eastern edge of the North Atlantic to provide the net northward geostrophic transport required to balance the southward Sverdrup transport of the interior. This transport is large enough to force the thermocline to surface and the western boundary current to separate from the continental margin. The latitude at which the current separates thus depends on the magnitude and structure of the wind stress curl over the basin.

During 1975 through 1978, the Stream apparently separated from the continental margin at a fixed point, Fig. 8. The continental margin turns northward downstream of SP, presumably inhibiting the tendency of the SP to migrate northward in response to changes in basin-wide forcing. Since basin-wide forcing mechanisms have a large annual cycle (Kutalo, 1971), a larger annual cycle than observed in the meander amplitude might be expected, if these were the dominant forcing mechanisms and there were not ameliorating factors.

To assess the importance of local path dynamics, we attempted to compare the steady inertial jet theory (Warren, 1963), which relates the path of the Stream to topographic steering, β effects and inertial effects, to our results. The results of the comparison are not presented because the inertial jet theory does not take into account other factors, such as the energetic eddy field in the vicinity of the Stream, now considered to be important (P. P. Niiler, personal communication, 1982). Variable wind stress curl and thermalhaline forcing in the vicinity of the Stream also have not been taken into account. We therefore could not adequately evaluate the relative importance of the above mechanisms in driving the standing meander. However, the present effort serves to identify the need for more comprehensive studies to understand the long-period standing meanders and the determinants of the SP.

6. Short-period propagating meanders

a. Basic characteristics of the meanders

Propagating meander time series were reconstructed by summing Modes 1–13, excluding Mode 4. These time series contained 81% of the total variance of the Stream path. Modes 14 and 15 were previously analyzed as upstream (from SP) standing meanders. Modes 16–34 were not used because their spatial structures were disorganized, and their time varying amplitudes were mainly white noise.

The standard deviation and extreme position envelopes around the mean position of the front due to the propagating meanders (Fig. 10) illustrate the typical growth of the meanders downstream of SP. The growth was rapid from the first 150 km downstream to the region where the capture of warm-core eddies was frequent (Fig. 2). Downstream of this region, the standard deviation increased slowly to about 70°W (near y = 540 km), then increased more rapidly farther downstream. The variance also increased slightly upstream of SP. At y = 0 the time series accounted for 22% of the total variance, indicating that some of the meander energy may originate in the

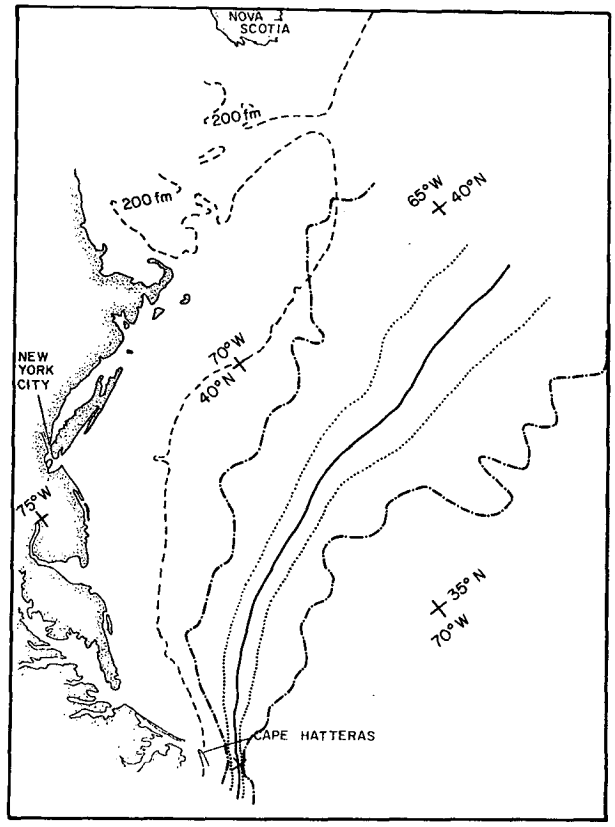

FIG. 10. Mean position (solid line), standard deviation envelope (dotted line), and extreme position envelope (dash-dot line) of the propagating meander time series.

South Atlantic Bight as coastally-trapped waves (Niiler and Mysak, 1971).

b. Estimated meander parameters

Using the method of Pratt (1976), wavenumber-frequency autospectra were computed and the spectra due to propagating and standing waves were separated (Fig. 11). (The order of calculation was not inverted here as in HM.) The total autospectrum (Fig. 11a) and the propagating wave autospectrum (Fig. 11b) are analyzed; the standing wave autospectrum is not, since it was not energetic for the propagating meander time series.

A cosine taper was applied in the time domain to the first and last 10% of each input time series, and smoothing was performed in the frequency domain by boxcar averaging. The number of degrees of freedom was 30 in the frequency domain. The spectra were computed for the alongstream interval $240 \leq y \leq 990$ km (subdomains 3 and 4), i.e., downstream of the region of frequent capture of warm-core eddies (Fig. 2). (Spectra computed for subdomain 3 alone had a very similar distribution of variance in wavenumber–frequency space. Hence, the frequent formation and capture of eddies in subdomain 4 apparently did not substantially affect the spectral properties.)

The total autospectrum was analyzed as a function of positive frequency (σ) and both positive and negative wavenumber (k) (Fig. 11a). (The spectrum at negative frequencies contained redundant information.) Substantial variance existed over the entire range of frequencies for wavelengths from 100 to several hundred km, which is evidence that we have completely determined the energetic wavenumber band, but not the frequency band, of the meanders. The variance was greater for positive wavenumbers than for negative. Since the propagating wave autospectrum for a given frequency equals the spectrum estimates for positive wavenumbers minus those for negative wavenumbers, substantial variance due to downstream-propagating meanders was present (Fig. 11b).

At less than 19 cpy, the propagating wave spectrum was mainly positive, indicating that downstream-propagating meanders dominated. Some variance due to upstream-propagating meanders was present at higher frequencies, where the signal-to-noise ratio was relatively poor. Therefore, our results were probably not reliable at these high frequencies. There was little variance due to propagating meanders with

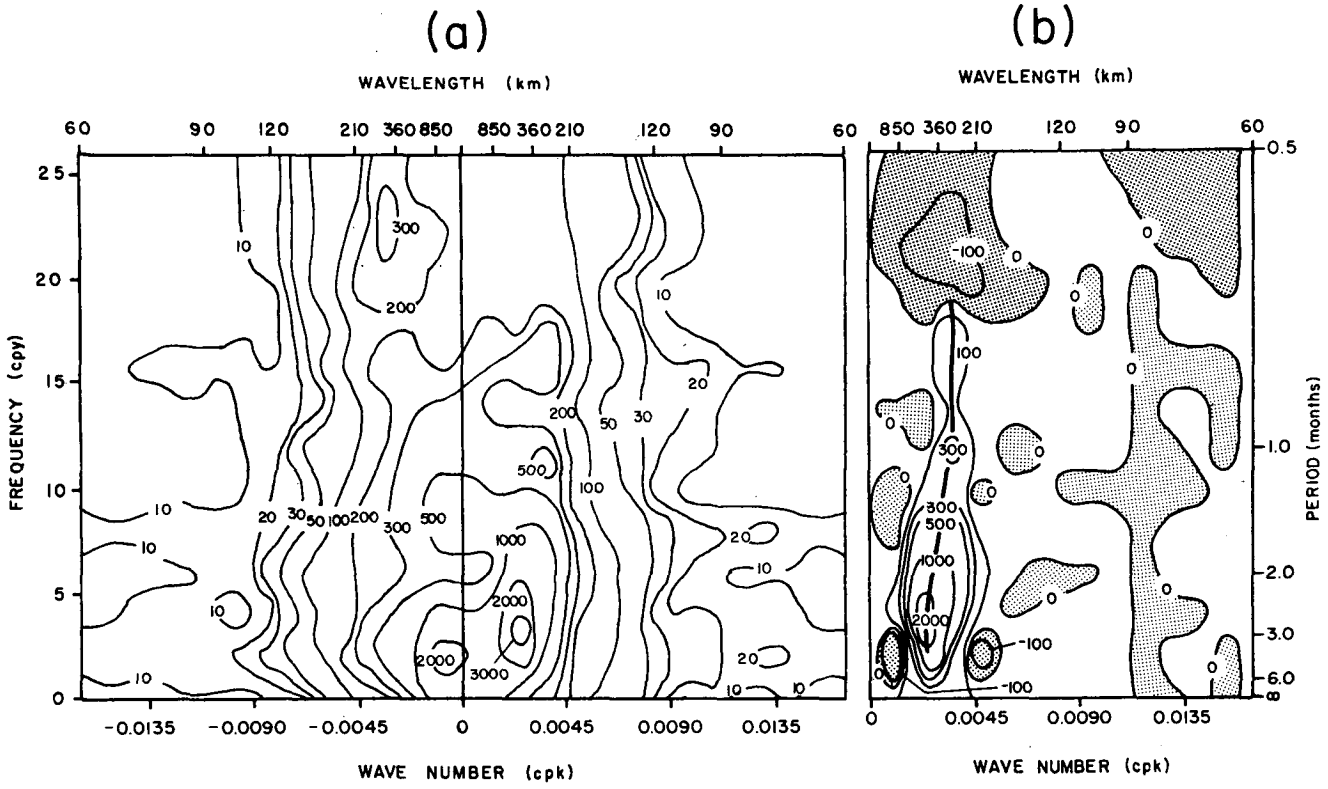

FIG. 11. Wavenumber-frequency autospectra of the propagating meander time series ($240 \leq y \leq 990$ km): (a) Total autospectrum; (b) propagating wave autospectrum. The maximum ridge in the propagating autospectrum is shown by the thick line. Contours are in $km^2\ cpw^{-1}\ cpk^{-1} \times 10^{-3}$.

wavelengths less than 200 km. Theoretically, random noise variance is equally distributed between positive and negative wavenumbers (Pratt, 1976). Thus, only the bias introduced by the human analyst of the EOFA charts, which we cannot quantify, could bias the propagating wave spectrum. We show later that this bias was probably small.

A statistical summary of the propagating meander characteristics obtained from Fig. 11b is presented in Table 3 for frequencies less than 18 cpy. For each frequency, the most energetic wavelength band was graphically read from Fig. 11b as defined by a factor of ten roll-off from the maximum energy density. The most energetic wavelength (indicated by the solid dark line in Fig. 11b) was also graphically estimated. By inspection of the error bars of the propagating autospectrum, it was determined that the uncertainty in the wavelength of maximum energy at each frequency was defined at a 95% confidence level by a factor of ⅓ roll-off from the maximum energy density (Table 3). The wavelength band was broadest between 2 and 8 cpy. The band narrowed substantially at higher frequencies. The most energetic wavelength was a maximum of 430 km at frequencies less than 4 cpy; it decreased with increasing frequency to 280 km for frequencies greater than 14 cpy. The resulting phase speed bands and phase speeds of the most energetic wavelength increased rapidly with frequency. [The 95% confidence limits for phase speeds were estimated from the confidence limits of the most-energetic wavelengths (Table 3).] In the most energetic frequency band of 2–10 cpy, phase speeds of the most energetic wavelengths ranged between 2.8 and 9.8 cm s^{-1}, with the total range of possible phase speeds between 1.6 and 15.8 cm s^{-1}.

Between ~200 and 300 km downstream of SP, Watts and Johns (1982) estimated phase speeds using the Inverted Echo Sounder (IES). Meander phase speeds increased from about 20 cm s^{-1} near 12 cpy to 42 cm s^{-1} near 90 cpy, indicating the phase speed increase with frequency (hence, the dispersive nature of propagating meanders) extended from 2–90 cpy. The discrepancy between our measured phase speed at 12 cpy (11 cm s^{-1}) and the 20 cm s^{-1} estimated by Watts and Johns may have resulted because our spectra were dominated by larger-amplitude, apparently shorter-wavelength meanders downstream of the IES array.

Group speeds were also estimated from $c_g = \partial\sigma/\partial k$ using the most energetic wavelength, Table 3. A statistically significant group speed could only be estimated for a broad frequency band due to the uncertainty in the estimates of these wavelengths. Group speed plus 95% confidence band was estimated to be 17 cm s^{-1} (11–25 cm s^{-1}) in the band 4 to 10 cpy. This band contained the most-energetic frequency band of the propagating meanders, which will be discussed later in more detail, and thus yielded the most reliable group speed estimates. This band also contained the dominant frequencies of the propagating meanders reported in Hansen (1970) (8 cpy) and in HM (6 cpy). Although we could not estimate it significantly, the group speed apparently increased at higher frequencies. Watts and Johns (1982) estimated a group speed of 47 cm s^{-1} for meanders of wavelength 330 km and frequency greater than 12 cpy. Since we could not adequately resolve group speed for frequencies greater than 12 cpy, their estimate of 47 cm s^{-1} could not be directly compared to our estimate of 17 cm s^{-1} for meanders between 4 and 10 cpy.

To estimate the overall most energetic wavelength and frequency of the propagating meanders from the present data, autospectra of the propagating meanders were computed by 1) integrating the wavenumber–frequency total and propagating wave autospectra over wavenumber and then multiplying the resulting frequency energy density spectra by 2.303σ, and 2) integrating the wavenumber–frequency total and propagating wave autospectra over frequency and then multiplying the resulting wavenumber energy density spectra by $2.303k$. When these integrated

TABLE 3. Summary of propagating meander characteristics obtained from the wavenumber-frequency propagating autospectrum. Group speed was computed from the rate of change of the most energetic wavelength with frequency between 4 and 10 cpy. Only frequencies at which downstream-propagating meanders dominated are shown. 95% confidence limits on the most-energetic wavelengths and corresponding phase speeds are given in parentheses. All estimated wavelengths are rounded to the nearest 10 km.

Frequency (cpy)	Wavelength band (km)	Most-energetic wavelength (km)	Phase speed band (cm s^{-1})	Phase speed at most-energetic wavelength (cm s^{-1})	Group speed (cm s^{-1})
2	250–600	450 (380–480)	1.6–3.8	2.8 (2.5–3.2)	
4	200–1000	430 (390–480)	2.6–14.6	5.5 (4.9–6.1)	
6	180–850	410 (350–480)	3.4–18.8	7.8 (6.6–9.1)	
8	200–650	360 (290–440)	5.0–16.5	9.1 (7.4–11.3)	17 (11–25)
10	200–500	310 (280–330)	6.4–15.8	9.8 (9.2–10.9)	
12	200–420	290 (260–320)	7.6–16.0	11.0 (10.0–12.3)	
14	250–360	280 (260–300)	11.1–16.0	12.4 (11.6–13.4)	
16	200–400	280 (260–300)	10.1–20.3	14.2 (13.3–15.3)	
18	200–400	280 (260–300)	11.4–22.8	16.0 (14.9–17.2)	

spectra are plotted linearly versus logσ and log$k$, respectively (Fig. 12a, b), the variance in any frequency or wavenumber band is proportional to the area under the respective curve within that band.

About 70% of the total variance was cancelled in computing the propagating wave autospectra (Fig. 12). From the integrated propagating wave spectra, substantial variance was present over the entire frequency band from 2 to 26 cpy, but most of the wavenumber variance was confined to meanders with wavelengths between 200 and 800 km. The complete wavenumber band of propagating meanders was fairly well determined, but the high frequency cutoff of propagating meanders was not. The most energetic frequency was 8 cpy, which was contained in a relatively energetic band between 4 and 9 cpy (Fig. 12a). This peak was significant at the 95% level of confidence for the integrated propagating wave frequency spectrum only, illustrating the effects of noise cancellation in the propagating wave spectrum.

The most energetic wavelength was about 330 km (Fig. 12b). Because of the relatively poor wavenumber resolution, this value was chosen such that half the propagating wave variance existed at longer wavelengths. The range of uncertainty in this wavelength estimate is probably a few tens of kilometers. Our estimates of the most energetic wavelength (330 km) and frequency (8 cpy) were virtually identical to the average wavelength and frequency estimated by Hansen (1970) and the wavelength estimated by Niiler and Robinson (1967). Interestingly, an energetic eddy field, based on current measurements within 1 km above the bottom, exists beneath the Stream south of New England (Luyten, 1977). Bursts of current with typically 30 day duration occurred every 1–3 months; therefore, the energetic frequency band of these deep eddies was similar to the energetic band of the propagating path meanders.

To search for the fundamental wavelength and frequency of the propagating meanders, empirical orthogonal functions in the frequency domain (*cf.* Wallace and Dickinson, 1972; Wang and Mooers, 1977; Halliwell, 1979) were computed for several frequency bands. For a specified frequency band and n input time series, n complex modes can be computed. The complex modes, i.e., eigenvectors, define an amplitude and phase relationship among the time series. Spatially coherent propagating waves can be isolated in separate frequency-domain EOF's which is impossible with time-domain EOF's.

EOF's in the frequency domain were computed in several frequency bands. The propagating meander time series were smoothed over 60 km alongstream intervals centered at y = 210, 300, 390, . . . , 930 km to reduce computational effort. The resulting Nyquist wavelength was 180 km, small enough to resolve the

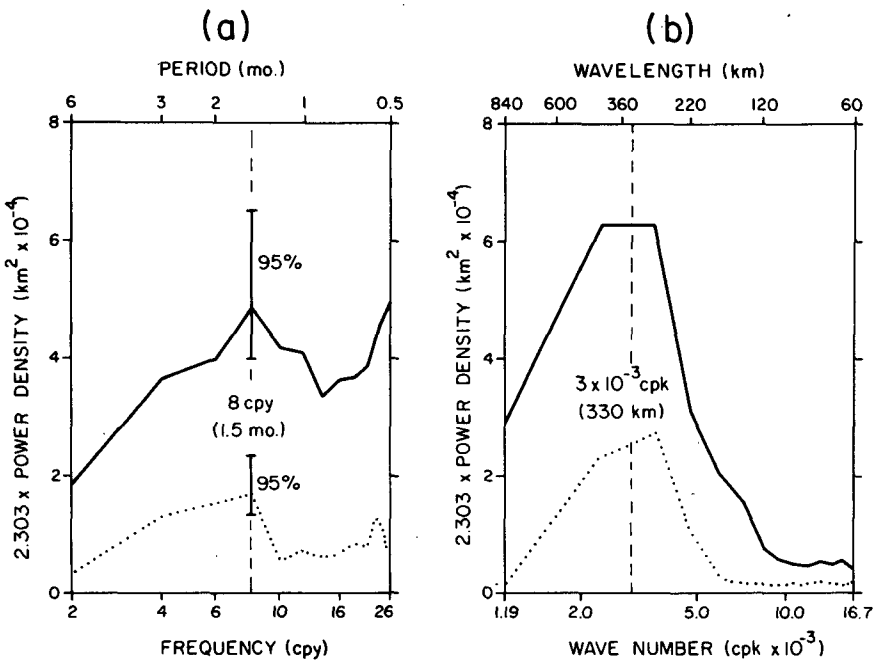

FIG. 12. Distribution of total variance of the propagating meander time series in the frequency and wavenumber domains: (a) 2.303× frequency × energy density, (b) 2.303 × wavenumber × energy density. The solid lines are total variance, and the dotted lines are the propagating wave variance. The variance within a specified frequency or wavenumber band equals the area beneath the appropriate curve. The most energetic frequency and wavenumber are marked by the vertical dashed lines.

energetic propgating meanders. The modes were only computed for $210 \leqslant y \leqslant 930$ km (subdomains 3 and 4).

The most significant modes had well-organized spatial structure over the entire alongstream domain only between 4 and 9 cpy, which corresponded to the relatively energetic band of the propagating wave variance (Fig. 12a). At other frequencies, the modes were coherent on scales small compared to the alongstream domain. For the higher frequencies, this was probably the effect of a poorer signal-to-noise ratio.

The most significant EOF modes in three frequency bands (4.0–4.5 cpy, 5.2–5.8 cpy, and 6.5–8.5 cpy) were used to study the properties of the meanders (Fig. 13 and Table 4). The amplitude within each frequency band was approximately equal, with an amplitude of ~2 km near $y = 210$ km, increasing approximately exponentially to more than 20 km near $y = 930$ km. An exponential function was fit to the data, resulting in an amplitude A of

$$A = 2.2 \exp[3.2 \times 10^{-3}(y - 210)] \text{ km}.$$

Thus, the exponential growth rate averaged $3.2 \pm 1.3 \times 10^{-3}$ km^{-1} for these frequency bands, which was somewhat larger than the estimate of Hansen (1970) of $2 \pm 1 \times 10^{-3}$ km^{-1}.

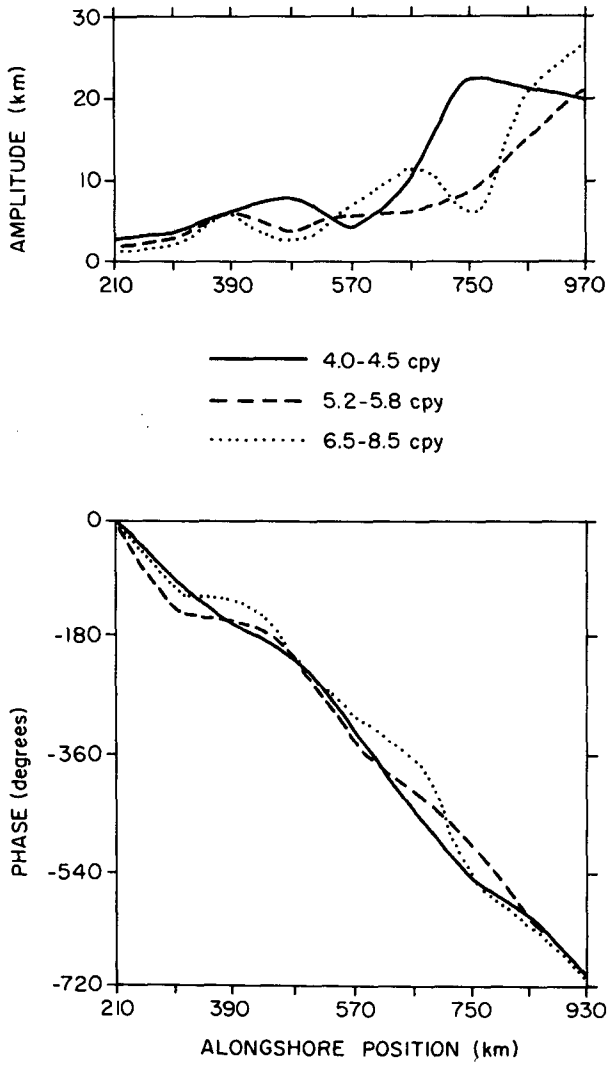

FIG. 13. Amplitude and phase of the most significant frequency domain EOFs for three frequency bands of the propagating meander time series.

TABLE 4. Meander parameters computed from the first EOF in the frequency domain for three frequency bands.

Frequency band (cpy)	Period band (weeks)	Percent variance explained	Wavelength $y > 480$ km (km)	Phase speed $y > 480$ km (cm s^{-1})
4.0–4.5	13.0–12.3	83	330	4.2–4.4
5.2–5.8	9.9–9.0	75	330	5.5–6.1
6.5–8.5	8.0–6.1	59	330	6.8–8.9

The slopes of the three phase functions were irregular for $y < 480$ km, where the meander amplitude was relatively small, and constant for $y > 480$ km. All meander parameters based on the phase were thus estimated for the subdomain $480 \leqslant y \leqslant 930$ km. The average wavelength estimated from the slope of the phase function was 330 km for each of the three frequency bands. Phase speeds (Table 4) computed from these wavelengths and frequencies therefore again increased substantially with increasing frequency. The wavelength and phase speed did not change substantially downstream as the amplitude of the meanders became large. The phase speed did not decrease as the amplitude increased as expected from nonlinear theory (Pedlosky, 1970; Ikeda, 1981).

A crude attempt was made to estimate the signal-to-noise ratio in these frequency bands in order to assess the significance of the frequency domain EOF's. We assumed the noise to be white and randomly distributed. We assumed the rms noise amplitude to be 30 km which is larger than the accuracy estimate of Perchal (1976).

The estimated rms noise levels were 4 km in the 4.0–4.5 cpy band, 5 km in the 5.2–5.8 cpy band, and 8 km in the 6.5–8.5 cpy band. For $y > 350$ km, the rms amplitudes of the three frequency domain modes were equal to or greater than the rms noise level (Fig. 13). The signal-to-noise ratio increased to 3 or 4 near the downstream end of the analysis domain. We felt confident that the relatively good signal-to-noise ratio allowed a reasonably accurate determination of the average parameters of the dominant meanders. The excellent agreement of wavelength and propagation speed with those determined by Hansen (1970) again indicated that subjective bias in the EOFA data was probably small.

The wavelength of the dominant modes, 330 km, equaled the most energetic wavelength previously estimated (Fig. 12b). The 6.5–8.5 cpy band contained

the most energetic frequency (8 cpy) previously estimated (Fig. 12a). Meanders with a predominant wavelength averaging about 330 km, a predominant frequency averaging about 8 cpy and a resulting phase speed of about 8 cm s^{-1} were apparently the most unstable meanders of the Gulf Stream path at periods greater than two weeks. Owing to variable inter-meander time scales, there were both substantial variance and coherent frequency domain EOF's with a wavelength of 330 km at frequencies as low as 4 cpy. Due to variable wavelength and propagation speed among meanders, variable inter-meander space and time scales, and the presence of higher-frequency energy (caused, for example, by the sudden appearances and disappearances of meanders associated with formation and capture of eddies), the propagating autospectrum was broadbanded (Fig. 11b).

We will not attempt to compare our analysis to existing theoretical models. No existing model is fully adequate to describe the dynamics of propagating meanders downstream of the SP. However, Hansen (1970) and Niiler (1975) made comparisons of several meander (unstable wave) models and observations, with some rough agreement achieved. The more promising models, including those of Orlanski (1969), Nitikin and Tareyev (1972), and Holland and Haidvogel (1980), contain the mechanisms for mixed barotropic-baroclinic instability. Propagating meanders are apparently sensitive to other factors, such as bottom slope, the beta effect, and frictional effects. The results of the present study are basically consistent with previous observational and theoretical studies, but they provide even more information on meander parameters to guide future theoretical work.

c. *Alongstream and temporal changes in meander parameters*

To search for possible alongstream changes in meander parameters, space-time autocorrelation functions were computed separately for subdomains 3 and 4 (Figs. 14a and b). The computational procedure was outlined in HM. (These functions are presented because wavenumber resolution was rather poor in wavenumber-frequency autospectra computed for individual subdomains.) Integral correlation time scales were estimated by integrating the function at zero lag distance from zero lag time to

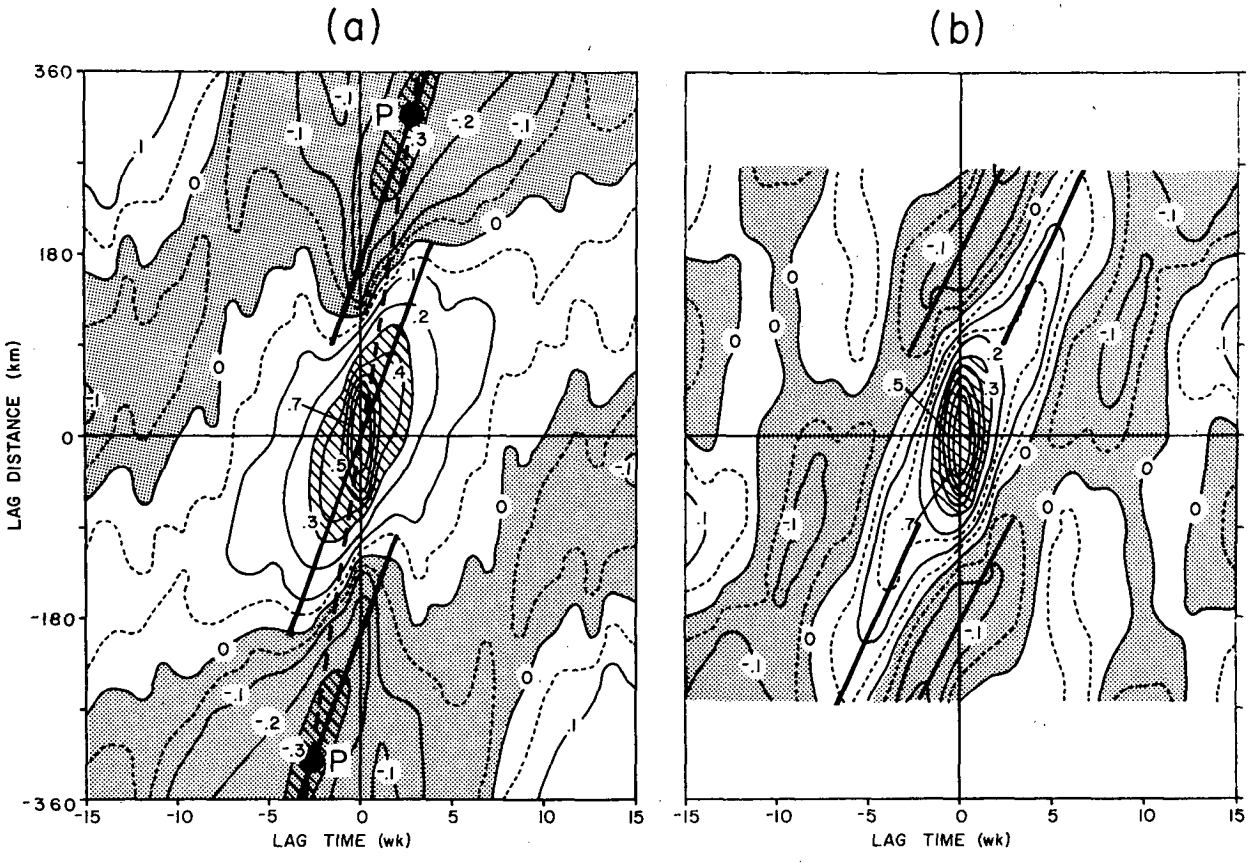

FIG. 14. Space-time autocorrelation functions of the propagating meander time series: (a) $240 \leq y \leq 690$ km; (b) $690 \leq y \leq 990$ km. Phase speed is equal to the slope of the thick solid lines and group speed is equal to the slope of the thick dashed lines. Correlation minima are indicated by the points P. Regions with correlation magnitude > 0.3 are cross-hatched to enhance ridges and troughs.

TABLE 5. Summary of parameters obtained from space-time autocorrelation functions.

Subdomain	Spatial correlation scale (km)	Temporal correlation scale (weeks)	Phase speed (cm s^{-1})	Group speed (cm s^{-1})	Wavelength (km)
(y = 240–690 km)	67	2.6	8	15	330
(y = 690–990 km)	66	1.8	6	...	330

the first zero crossing at positive lag time. Integral correlation space scales were estimated by integrating the function at zero lag time from zero lag distance to the first zero crossing at positive lag distance. Average phase speed was estimated from the slope of ridges and troughs of the correlation functions, indicated by the solid dark lines in Fig. 14. Wavelengths were estimated from the lag separation distance between the solid dark lines marking the two correlation troughs in both Figs. 14a, b. Group speed was estimated for subdomain 3 only from the slope of the dashed dark line connecting the correlation maximum at zero lag distance and lag time with the correlation minima indicated by the points "P" in Fig. 14a. (The correlation minima could not be located in Fig. 14b due to insufficient maximum lag distance; hence, a group speed estimate was not made for subdomain 4.) The slope of the line connecting these correlation extrema essentially gives the speed at which meander energy propagates. All parameters estimated from Fig. 14 are summarized in Table 5.

The change in spatial correlation scale was insignificant between the two subdomains (67 km in subdomain 3 and 66 km in subdomain 4). The temporal correlation scale was substantially smaller in subdomain 4 (1.8 weeks) than in subdomain 3 (2.6 weeks), which could have resulted from more-frequent sudden appearances and disappearances of meanders in subdomain 4 due to formation and capture of eddies. These correlation scales defined minimum sampling intervals in space and time required to fully sample these propagating meanders in future studies. In this study, the sampling intervals were about one-half of the ideal minima in both space and time. (The temporal sampling interval would have to be increased, however, to study the less-energetic propagating meanders with periods less than two weeks.)

The average phase speed decreased downstream from 8 cm s^{-1} in subdomain 3 to 6.5 cm s^{-1} in subdomain 4. Although the propagation speeds of the dominant spatially-coherent meanders between frequencies of 4 and 9 cpy did not decrease downstream (Fig. 13), the average meander propagation speed over all frequencies and wavenumbers did decrease downstream which was consistent with the predictions of nonlinear theory. Group speed averaged 15 cm s^{-1} in subdomain 3. (Even though it could not be estimated in subdomain 4 due to insufficient maximum lag distance, it appears from the correlation pattern in Fig. 14b that a similar group speed exists in subdomain 4.) The dispersive nature of the meanders was also revealed by the decrease in phase speed for lag time greater than 3 weeks in subdomain 3. Dispersion was less evident in subdomain 4. Wavelengths averaged 330 km in both subdomains.

To analyze the temporal variability of correlation scales and phase speeds (Table 6), space-time autocorrelation functions (not shown) were computed over subdomains 3 and 4 for eight 6-month time intervals during the four-year study. There was substantial temporal variability in these meander statistics. Six-month averaged phase speeds ranged from 2.6–19.2 cm s^{-1}, temporal correlation scales from 0.6 to 5.8 weeks, and spatial correlation scales from 48 to 99 km.

The amplitude of propagating meanders also has substantial temporal variability, as measured by the meander amplitude index m (Fig. 15), computed from the propagating meander time series by

$$m = (l - 990)/990,$$

where l is the arc length of the Stream within the entire 990 km alongstream domain. If the Gulf Stream front was located along a line of constant y throughout the alongstream domain, the value of m would be zero. Since the reconstructed propagating meander time series had zero mean, the additional arc length due to the curved mean path was not present in the computed index.

TABLE 6. Six-month averages of Gulf Stream meander parameters computed from space-time autocorrelation functions.

	1975		1976		1977		1978	
Parameter	Jan–Jun	Jul–Dec	Jan–Jun	Jul–Dec	Jan–Jun	Jul–Dec	Jan–Jun	Jul–Dec
Phase speed (cm s^{-1})	10.8	2.6	8.5	19.2	8.6	4.3	8.5	3.1
Alongstream correlation scale (km)	62	78	72	99	67	54	48	78
Temporal correlation scale (weeks)	1.0	5.8	2.0	3.0	1.7	0.6	2.1	4.9

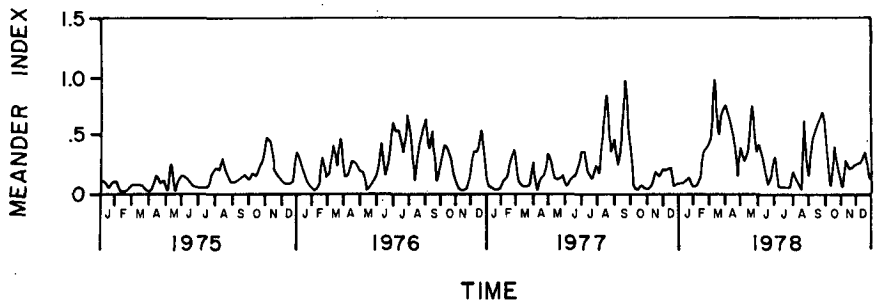

FIG. 15. Gulf Stream propagating meander amplitude index.

During the first two-thirds of 1975, the index was very small; large-amplitude meanders were not common during this time interval. There were periods of sustained large-amplitude meanders, such as during summer 1976, August and September 1977, and February–May 1978. The index was very small from October 1977–January 1978. No warm-core eddies were formed during this latter quiescent period, which led to an interval of several weeks when no warm-core eddies were observed between Cape Hatteras and the Northeast Channel. The autospectrum of m (not shown) indicated substantial variance at periods greater than three months. There was no distinct annual peak, but there may have been a weak annual cycle, Table 2. The monthly averages were smallest in January and February (0.12 and 0.16), and largest in August and September (0.35 and 0.43).

7. Discussion

The Gulf Stream begins to turn seaward at a point southeast of Cape Hatteras near 35°20′N, 74°50′W. This separation point (SP) is the demarcation between the South Atlantic Bight regime, where the Stream flows along the continental margin, and the open-ocean regime where the Stream path is not constrained by lateral boundaries. A relative alongstream maximum in bottom slope and a relative alongstream minimum in the variance of path fluctuations occur at this point. The separation is aided by the downstream cyclonic curvature of isobaths. Meander characteristics differ substantially upstream and downstream of SP.

At periods greater than two weeks, two meander modes dominated the path variability downstream of Cape Hatteras from 1975 through 1978. At periods greater than four months, the first meander mode, a standing path meander, existed in the first 600 km downstream of SP. This meander was confined between two nodes, one at SP and the other at 38°15′N, 68°12′W (about 200 km south of the western end of Georges Bank). At the antinode, located midway between the two nodes (south of New England), the rms amplitude was 36 km with extreme path excursions of $\sim \pm 90$ km.

The second meander mode was that of downstream-propagating meanders. They were energetic at periods ranging from the Nyquist period of two weeks to a few months. Amplitudes of these meanders could exceed 200 km, and the meanders often detached from the Stream to form warm and cold core eddies. The dominant wavelength and frequency averaged 330 km and 8 cpy with a resulting phase speed of 8 cm s^{-1}. The meanders had a (downstream) group speed of about 17 cm s^{-1} and grew exponentially in the first 900 km downstream of SP, with a spatial growth rate averaging 3.2×10^{-3} km^{-1}. Owing to variable wavelength and propagation speed among meanders, variable inter-meander space and time scales, and the presence of higher-frequency variance (due, for example, to the sudden appearance and disappearance of meanders because of the formation and capture of eddies), meanders were energetic over a broad wavenumber-frequency band. The band narrowed and shifted to larger wavenumbers with increasing frequency. The most energetic wavenumber also increased with increasing frequency. Phase speed was therefore frequency dependent, increasing from 3 to 16 cm s^{-1} between 2 and 18 cpy. At 4–6 cpy the energetic wavelength band was 200 to more than 800 km, and, at frequencies greater than 12 cpy, the band was 200 to about 400 km. There was substantial variability in the frequency of formation of propagating meanders, and in their amplitudes, at periods greater than three months.

Since this data set extended only 60 km upstream of SP, we could not fully study Gulf Stream meanders in the South Atlantic Bight. There was apparently an energetic meander at periods greater than three months in the 60 km interval with a downstream node at SP. It was apparently unrelated to the standing meander downstream of SP. A study should be undertaken in the South Atlantic Bight using the southern EOFA chart to determine the structure of this meander. However, such a study would not resolve the most energetic downstream-propagating meanders in the South Atlantic Bight, since they occur at periods shorter than the EOFA's (Nyquist *et al.*, 1977).

A weak annual cycle was noted in the Stream path. Its relationship to the annual cycle of transport in the Gulf Stream system as documented in earlier studies, is indeterminant from the present study.

The long-period standing meander downstream of SP could have a substantial effect on the oceanic and atmospheric conditions of the northwest Atlantic. The Gulf Stream and adjacent Sargasso Sea region has strong sea-to-air exchange of heat and is the site of formation of 18°C water in winter. Shoreward excursions of the Stream path bring Gulf Stream and Sargasso Sea water closer to the cold continental air that frequently flows offshore, which could affect the water mass formation process. Similarly, shoreward excursions could allow coastal atmospheric cyclones to intensify more rapidly as they propagate northeastward along the Middle Atlantic and New England coast. For example, during the winter of 1977–78, when the Stream was close to the shoreward extreme path of the standing meander, intense cyclones were common off the northeast United States. It may be of interest, in a future study, to demonstrate the relative importance of the meander to this phenomenon.

The results of this study indicate that satellite-derived data of Gulf Stream positions, even relatively noisy time series obtained from thermal IR images, can be usefully applied to study Gulf Stream path variability. Due to frequent cloud cover problems, more frequent sampling rates than once per week, as available in this study, may not be realistically achieved over a long period of time from IR imagery alone. Despite this limitation, the satellite-derived IR data described the variability in the Gulf Stream path at periods greater than two weeks with reasonable accuracy.

This study could be extended in space and time. The southern EOFA chart can be used to extend the study to the South Atlantic Bight, and EOFA data both upstream and downstream of Cape Hatteras can be employed through early 1980 when they were discontinued. Continuation beyond this time could be achieved by using oceanographic analysis charts currently produced by the National Weather Service (Auer, 1980). Extension in time is important because the long-period cutoff of the standing meander downstream of SP was not resolved with our four-year data set. Ultimately, these data should be combined with wind stress curl data evaluated over the North Atlantic Basin and sea levels in the North Atlantic Ocean, Caribbean Sea, and Gulf of Mexico to study the response of the subtropical gyre and its western boundary current to large-scale atmospheric forcing. In the future, it would be extremely promising to combine these analyses of the Gulf Stream front locus with other conventional oceanographic data sets bearing on the Gulf Stream and its variability.

Acknowledgments. The authors thank Mr. J. Lockwood Chamberlin for helpful discussions concerning the EOFA charts, and for suggesting the Gulf Stream meander amplitude index. Doctors R. W. Garvine, P. P. Niiler, A. R. Robinson and J. S. Allen provided helpful comments. Mr. Rudy Perchal is again thanked for providing the NAVOCEANO EOFA charts and for helpful discussions on their construction.

This work was supported under Subcontract C66007 from EG&G, Environmental Consultants to the University of Delaware, as part of the ongoing New England Outer Continental Shelf Program of the Bureau of Land Management. Part of the work was completed at Oregon State University under Subcontract B118584 from the University of Delaware and at the Naval Postgraduate School under ONR Research Projects RR031-01-01 and RR031-02-01.

REFERENCES

Auer, S., 1980: New daily oceanographic analyses. *Gulfstream,* **6,** 3.

Charney, J. G., 1955: The Gulf Stream as an inertial boundary layer. *Proc. Nat. Acad. Sci.,* **41,** 731–740.

Curtin, T. B., L. J. Pietrafesa and N. E. Huang, 1978: Concurrent satellite and ship observations across the Gulf Stream north of Cape Hatteras. Dept. Mar. Sci. Eng., Tech. Rep. 78-4, North Carolina State University, 26 pp.

Fuglister, F. C., 1951: Annual variations in current speeds in the Gulf Stream system. *J. Mar. Res.,* **10,** 119–127.

——, and A. D. Voorhis, 1965: A new method of tracking the Gulf Stream. *Limnol. Oceanogr.,* **10**(Suppl.), R115–R124.

Halliwell, G. R., Jr., 1979: The space-time structure and variability of the shelf water/slope water and Gulf Stream surface thermal fronts, and warm-core eddies, off the northeast U.S. MS thesis, Tech. Rep. CMS-C-2-78, College of Marine Studies, University of Delaware, 195 pp.

——, and C. N. K. Mooers, 1979: The space-time structure and variability of the shelf water-slope water and Gulf Stream surface temperature fronts, and associated warm-core eddies. *J. Geophys. Res.,* **84,** 7707–7726.

Hansen, D. V., 1970: Gulf Stream meanders between Cape Hatteras and the Grand Banks. *Deep-Sea Res.,* **17,** 495–511.

——, and G. A. Maul, 1970: A note on the use of sea surface temperatures for observing ocean currents. *Remote Sens. Environ.,* **1,** 161–164.

Holland, W. R., and D. B. Haidvogel, 1980: A parameter study of the mixed instability of idealized ocean currents. *Dyn. Atmos. Oceans,* **4,** 185–215.

Ikeda, M., 1981: Meanders and detached eddies of a strong eastward-flowing jet using a two-layer, quasi-geostrophic model. *J. Phys. Oceanogr.,* **11,** 526–540.

Kutalo, A. A., 1971: On seasonal changes in the North Atlantic circulation. *Izv. Atmos. Oceanic Phys.,* **1,** 208–213.

Lee, T. N., and D. A. Mayer, 1977: Low-frequency current variability and spin-off eddies along the shelf of southeast Florida. *J. Mar. Res.,* **35,** 193–220.

Leetmaa, A., and A. F. Bunker, 1978: Updated charts of the mean annual wind stress, convergences in the Ekman layers, and Sverdrup transports in the North Atlantic. *J. Mar. Res.,* **36,** 311–322.

Luyten, J. R., 1977: Scales of motion in the deep Gulf Stream and across the continental rise. *J. Mar. Res.,* **35,** 49–74.

Maul, G. A., 1977: The annual cycle of the Gulf Loop Current, I, Observations during a one year time series. *J. Mar. Res.,* **35,** 29–47.

——, P. W. deWitt, A. Yanaway and S. R. Baig, 1978: Geostationary satellite observations of Gulf Stream meanders: infrared measurements and time series analysis. *J. Geophys. Res.*, **83,** 6123–6135.

Morgan, G. W., 1965: On the wind-driven ocean circulation. *Tellus,* **8,** 301–320.

Niiler, P. P., 1975: Variability in western boundary currents. *Numerical Models of Ocean Circulation,* Nat. Acad. Sci., Washington, DC, 216–235.

——, and L. A. Mysak, 1971: Barotropic waves along an eastern continental shelf. *Geophys. Fluid Dyn.*, **2,** 273–288.

——, and A. R. Robinson, 1967: The theory of free inertial jets. II: A numerical experiment for the path of the Gulf Stream. *Tellus,* **19,** 601–618.

Nikitin, O. P., and B. A. Tareyev, 1972: Meanders of the Gulf Stream interpreted as resultants of baroclinic instability predicted by a simple two-layer model. *Izv. Atmos. Ocean. Phys.*, **8,** 973–980.

Orlanski, I., 1969: The influence of bottom topography on the stability of jets in a baroclinic fluid. *J. Atmos. Sci.*, **26,** 1216–1232.

Otnes, R. M., and L. Enochson, 1978: *Applied Time Series Analysis.* Wiley and Sons, 449 pp.

Parker, C. E., 1976: Some effects of lateral shifts of the Gulf Stream on the circulation northeast of Cape Hatteras. *Deep-Sea Res.*, **23,** 795–803.

Pedlosky, J., 1970: Finite-amplitude baroclinic waves. *J. Atmos. Sci.*, **27,** 15–27.

Perchal, R. J., 1976: Comparison of Gulf Stream eddies detected by airborne radiation thermometer and VHRR-IR satellite imagery during SUBASWEX 1-76. NAVOCEANO Tech. Note 3700-52-76, U.S. Naval Oceanographic Office, 21 pp.

Pratt, R. W., 1976: The interpretation of space-time spectral quantities. *J. Atmos. Sci.*, **33,** 1060–1066.

Robinson, A. R., J. R. Luyten and F. C. Fuglister, 1974: Transient Gulf Stream meandering. Part I: An observational experiment. *J. Phys. Oceanogr.*, **4,** 237–255.

Stommel, H., 1966: *The Gulf Stream.* University of California Press, 248 pp.

Veronis, G., 1973: Model of world ocean circulation. I: Wind-driven, two-layer. *J. Mar. Res.*, **31,** 228–288.

Wallace, J. M., and R. E. Dickinson, 1972: Empirical orthogonal representation of time series in the frequency domain. Part I: Theoretical considerations. *J. Appl. Meteor.*, **11,** 887–892.

Wang, D-P., and C. N. K. Mooers, 1977: Long coastal trapped waves off the west coast of the United States, summer 1973. *J. Phys. Oceanogr.*, **7,** 856–864.

Warren, B. A., 1963: Topographic influences on the path of the Gulf Stream. *Tellus,* **15,** 167–183.

Watts, D. R., and D. B. Olson, 1978: Gulf Stream ring coalescence with the Gulf Stream off Cape Hatteras. *Science,* **202,** 971–972.

——, and W. E. Johns, 1982: Gulf Stream meanders: Observations on propagation and growth. *J. Geophys. Res.*, **87,** 9467–9476.